Applied Surface Science 649 (2024) 159100

Contents lists available at ScienceDirect

Applied Surface Science

journal homepage: www.elsevier.com/locate/apsusc

Full Length Article

Oxidation-driven 2D LIPSS on amorphous Si films atop metal layers: The interplay of near-field and far-field effects

Liye Xu [a,b,c,d], Jiao Geng [e,f,*], Liping Shi [e,f], Weicheng Cui [c,d], Min Qiu [b,d,g,*]

[a] College of Information Science and Electronic Engineering, Zhejiang University, 866 Yuhangtang Rd, Hangzhou 310058, Zhejiang, China
[b] Key Laboratory of 3D Micro/Nano Fabrication and Characterization of Zhejiang Province, School of Engineering, Westlake University, 18 Shilongshan Rd, Hangzhou 310024, Zhejiang, China
[c] Key Laboratory of Coastal Environment and Resources of Zhejiang Province (KLaCER), School of Engineering, Westlake University, 18 Shilongshan Rd, Hangzhou 310024, Zhejiang, China
[d] Institute of Advanced Technology, Westlake Institute for Advanced Study, 18 Shilongshan Rd, Hangzhou 310024, Zhejiang, China
[e] Hangzhou Institute of Technology, Xidian University, 8 Qiannong East Rd, Hangzhou 311200, Zhejiang, China
[f] School of Optoelectronic Engineering, Xidian University, 2 South Taibai Rd, Xi'an 710071, Shaanxi, China
[g] Westlake Institute for Optoelectronics, Westlake University, 68 Jiangnan Rd, Hangzhou 311421, Zhejiang, China

ARTICLE INFO

Keywords:
Oxidation-Driven LIPSS
Near-field and far-field effects
Circularly polarized femtosecond laser

ABSTRACT

We investigate the formation of Laser-Induced Periodic Surface Structures (LIPSS) on amorphous Si films coated on Al using circularly polarized femtosecond lasers. By controlling laser fluence, we induce oxidation-based surface patterns, with their regularity governed by the interplay between near-field and far-field contributions. Achieving the right balance between these effects results in a consistent hexagonal pattern. Varying the underlying metal type further revealed its impact on pattern quality: strong far-field contributions led to irregular patterns, while dominant near-field effects resulted in extensive oxidation. Our study reveals the critical balance between near-field and far-field effects in optimizing 2D LIPSS patterns, emphasizing the role of the underlying metal.

1. Introduction

The realm of material surface modification has yielded fascinating properties, including rich and striking colors [1–3], hydrophobic surfaces [4–5] and biomimetic features [6]. Among the various methods, the fabrication of micro- and nano-scale texture structures arranged in a certain order on surfaces has garnered significant interest. These functional surfaces find wide applications in antibacterial [7], biosensing [8], solar cells [9–11], electronics [12] and photonics [13–14]. However, the quest for rapid fabrication of large-area and high-quality surface nanostructures remains a challenging pursuit.

Traditional methods, such as direct laser writing [15], laser interference lithography [16], two-photon polymerization [17], nanoimprinting lithography [18], electron beam lithography [19] and focused ion beam milling [20], have notable limitations, including high costs, slow fabrication speeds, extreme processing conditions, and cumbersome steps. As a promising alternative, laser-induced periodic surface structures (LIPSS) offer excellent robustness, cost-effectiveness, and simplicity.

Since its initial observation by Birnbaum [21] in 1965, numerous studies have focused on inducing grating-like one-dimensional (1D) LIPSS on various materials, including metals [5,22–24], semiconductors [22,25], polymers [26–29] and glasses [6]. The generation mechanism of LIPSS is typically attributed to the periodic distribution of energy resulting from the interference of incident light and surface electromagnetic waves excited by surface roughness [21,25,30–34]. Consequently, selective ablation of the material surface occurs [35–36]. However, under intense laser fluence, excessive heat and ablative remnants markedly perturb these waves, yielding LIPSS marred by irregularities, forks, and meanders [37].

In contrast, oxidation-based LIPSS, characterized by lower laser fluence and reduced redundant heat, exhibits a more gentle formation process, leading to significantly improved long-range regularity [37–42]. Unlike ablation-based LIPSS, the formation of oxidation-based

* Corresponding authors at: Hangzhou Institute of Technology, Xidian University, 8 Qiannong East Rd, Hangzhou 31200, Zhejiang, China (J. Geng). Key Laboratory of 3D Micro/Nano Fabrication and Characterization of Zhejiang Province, School of Engineering, Westlake University, 18 Shilongshan Rd, Hangzhou 310024, Zhejiang, China (M. Qiu).
E-mail addresses: gengjiao@xidian.edu.cn (J. Geng), qiumin@westlake.edu.cn (M. Qiu).

https://doi.org/10.1016/j.apsusc.2023.159100
Received 26 September 2023; Received in revised form 27 November 2023; Accepted 6 December 2023
Available online 12 December 2023

LIPSS is influenced not only by the interference of incident light and surface electromagnetic waves but also by the near-field effect. The near-field can facilitate the rapid growth and dominance of oxide particles, further enhancing the intensity of the far-field [34,37]. Moreover, the near-field effect even impacts the direction and quality of 1D LIPSS [34].

While substantial attention has been devoted to the fabrication of 1D LIPSS, recent scientific focus is shifting towards the emerging field of two-dimensional (2D) LIPSS. Typically, ablation-based 2D LIPSS is induced using two orthogonal linearly polarized laser pulses [23–24,43–44] or circularly polarized laser pulses [23–24,45–49]. However, the domain of oxidation-based 2D LIPSS, which may offer distinct advantages and phenomena due to the interplay of material transformation and laser-induced patterning, remains a largely uncharted territory in laser-materials interaction research.

In our study, we ventured into the induction of oxidation-based 2D LIPSS, showcasing a hexagonal configuration, on a 50-nm Si film layered on Al. This was achieved using circularly polarized femtosecond lasers, with a keen emphasis on fluence modulation. Our numerical simulations provided insights into the pattern's evolution, underscoring the critical balance between near-field and far-field effects. Furthermore, our exploration spanned the ramifications of varying the foundational metal substrate, elucidating the nuanced interplay of these effects in the context of oxidation-driven LIPSS formation. Our research contributes a novel perspective in the field of laser-induced periodic surface structures, particularly in the oxidation-based 2D LIPSS on Si films. This unique approach, focusing on hexagonal pattern formation through fluence modulation and the impact of different metal substrates, enriches the current understanding and opens new avenues for further exploration in this area.

2. Material and methods

2.1. Experimental setup

Experiments were conducted using a diode-pumped ultrafast fiber amplifier system (Amplitude) that emitted pulses of 130 fs duration at a 5 kHz repetition rate and a central wavelength of 1030 nm. Circularly polarized laser pulses were achieved using a quarter-wave plate. The laser was focused onto the sample, which was mounted on a 2D translation stage, using a 20 cm focal length converging lens. The laser spot diameter was approximately 95 μm verified by a laser beam profiler (Ophir Photonics). During experiments, the stage consistently moved at a speed of 20 μm/s, each point on the sample surface was subjected to approximately 23,750 pulses, ensuring a consistent pulse count across all fluence levels to isolate the effects of fluence on LIPSS formation. Laser fluence adjustments were made using a combination of a half-wave plate and a linear polarizer. The precise measurement of the laser power was conducted using a digital power and energy meter console (THORLABS PM100D) paired with a standard photodiode power sensor (THORLABS S120C), ensuring accurate control over the energy delivered to the sample surface. In reporting the laser fluence values, we have accounted for measurement uncertainties. The power meter used has a specified uncertainty of ± 7% at the wavelength of 1030 nm, and we estimate an additional error of approximately 3% for the area measurement based on the precision of the instrument used. The combined relative error in laser fluence measurement is thus estimated to be around 7.62%. These uncertainties are reflected in our analysis, ensuring that the trends observed are based on reliable relative comparisons.

2.2. Sample fabrication

The fabrication of the thin films was meticulously carried out using a magnetron sputtering system (ULVAC CS200Z) at room temperature. The substrates used were 2-inch single-crystalline silicon wafers. The detailed parameters for the sputtering of different films are provided in Table 1 below.

Table 1
Sputtering Parameters for Film Deposition.

Material	Au	Cu	Pt	Ti	Si
Sputtering Type	DC	DC	DC	DC	RF
Power(W)	100	600	100	600	300
Pressure(Pa)	0.3	0.3	0.3	0.3	0.3
Flow Rate of Ar (sccm)	150	100	150	150	70
Target Distance (mm)	130	130	130	130	90

Initially, the metal films (Gold, Copper, Platinum, and Titanium) were deposited under specific conditions, as outlined in the table. Following the deposition of these metal films, Silicon films were subsequently coated using RF sputtering. This sequential deposition process was vital to ensure the integrity and uniformity of the multi-layered thin films. Each step in the fabrication process was carefully controlled and monitored to maintain consistency in film quality.

2.3. Sample Characterization

The surface morphology and compositional analysis were assessed using a field-emission scanning electron microscope (Hitachi Regulus 8230) equipped with energy dispersive X-ray spectroscopy (EDX), allowing for high-resolution imaging and elemental identification. The thickness measurements of the amorphous silicon and metal films were precisely determined utilizing a Tencor P-7 stylus profiler, renowned for its accuracy in profiling surface topography. Additionally, atomic force microscopy (AFM) images were captured with a Dimension ICON AFM, providing nanoscale resolution of the surface structures.

2.4. Numerical simulations

The finite-difference-time-domain (FDTD) method, as implemented in the Lumerical FDTD solutions software package, was utilized to simulate electric field distributions during 2D-LIPSS growth. The simulated sample closely mirrored the experimental sample: a 50 nm thick Si top layer, a 100 nm thick metal middle layer, and a thick crystalline Si substrate at the bottom. This configuration was chosen to accurately reflect the physical conditions under which the LIPSS formed. SiO_2 particles, modeled as cylinders with a 150 nm depth and 200 nm diameter, were embedded in the top a-Si layer and extend 100 nm from the film surface. These particles were introduced into the simulations to represent surface impurities or defects, which are known to influence the deposition of electromagnetic wave energy and subsequently affect LIPSS formation. The dimensions of these particles were selected based on established literature [50], which suggests that particles of this size significantly modulate energy deposition on the surface.

In our simulations, we utilized a plane wave light source to model the incident laser irradiation. This approximation is commonly employed in computational electromagnetics for scenarios where the area of interest is significantly smaller than the beam size. It simplifies the computational model while still capturing the essential physics of the light-matter interaction.The plane wave source was positioned 2 μm above the sample surface, a choice made to prevent the simulation's boundary conditions from artificially affecting the field distribution near the sample. This setup ensures that the simulation results are not influenced by proximity to the domain boundaries and are thus more representative of the actual experimental conditions.While the experimental setup involves a focused laser beam with a finite width of 95 μm, the central region of a well-collimated and focused Gaussian beam can be closely approximated by a plane wave over a small simulation area. Our simulations focus on a 10 μm × 10 μm area, within which the plane wave approximation is valid and provides an accurate representation of the near-field effects that are critical for understanding LIPSS formation.

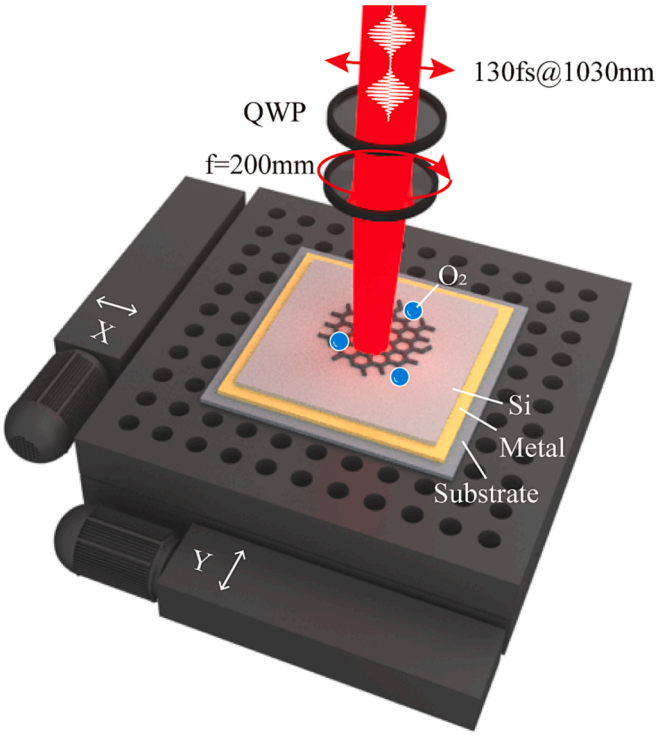

Fig. 1. Experimental setup. QWP: quarter-wave plate.

The simulation domain was a 10 μm × 10 μm × 2.5 μm (x × y × z) cuboid. Periodic boundary conditions were applied to the x- and y-axes to mimic an infinitely repeating structure. A perfectly matched layer (PML) was used along the z-axis to absorb outgoing waves and prevent reflections that could interfere with the simulation results. The mesh was set to an auto-nonuniform type to optimize accuracy and computational efficiency. A frequency-domain field and power monitor tracked the electric field at the Si-air interface, which is critical for understanding the LIPSS formation process. Simulations concluded once the energy within the domain dropped below a specified threshold (10^{-5}), ensuring that the results reflected a steady-state condition akin to the experimental observations. This approach allowed us to analyze the electric field distributions that contribute to the growth of 2D-LIPSS under various conditions, providing valuable insights into the underlying mechanisms of pattern formation.

3. Results and discussion

As shown in Fig. 1, utilizing a diode-pumped ultrafast fiber amplifier system, we irradiated a bilayer film composed of 100 nm metal and 50 nm amorphous Si with circularly polarized laser pulses of 130 fs duration. The aim was to induce oxidation patterns and study their formation and characteristics. The laser's influence on the film, combined with the specific properties of the chosen materials, set the stage for the observations and analysis that followed.

As depicted in Fig. 2, we successfully generated regular hexagonal oxidation patterns on a bilayer film, comprising 100 nm of Al and 50 nm of amorphous Si, using a circularly polarized laser with a pulse duration of 130 fs. Upon exposure to femtosecond laser pulses, this metal-Si composite underwent a distinct oxidation process. Guided by the combined effects of the laser's near-field and far-field, SiO_2 particles organized into specific patterns on the Si surface. The laser fluence critically influenced the 2D LIPSS's regularity. In Fig. 2 (a1), at a modest fluence of 22.58 mJ/cm^2, we primarily observed a skewed 1D LIPSS, interspersed with areas displaying irregular 2D configurations where adjacent stripes interconnected, yielding hole-like formations. These stripe orientations were discernible in the fast Fourier transform (FFT) map. As we increased the fluence, the prevalence of these hole structures grew, transitioning their arrangement from a more random to a structured hexagonal pattern. Upon reaching a fluence of 26.82 mJ/cm^2, as shown in Fig. 2 (d1), the configurations solidified into a definitive hexagonal shape, corroborated by the FFT map in Fig. 2 (d2). The inter-hole spacing measured approximately 931 nm, closely mirroring the periodicity of the grating structure observed under linear polarization. However, any further escalation in fluence disrupted this pattern's consistency, as shown in Fig. 2 (e1), initiating oxidation within the holes.

In contrast to the dewetting process observed in ablative LIPSS, the laser fluence employed to generate oxidative LIPSS wasn't sufficiently intense to melt the material [37]. This distinction means the formation of the regular oxidative hexagonal structure diverged from the processes dominated by ablation. Our prior studies [34,37] comprehensively detailed the genesis of the grating-like oxidative 1D LIPSS, prompted by a linearly polarized femtosecond laser on amorphous silicon (a-Si). With the initial laser pulse, surface defects triggered the excitation of surface-scattered waves, which, when interfered with the laser light, produced a periodic energy intensity distribution [34,51,52].

Fig. 3 (a) delves into the preliminary stages of this process under circular laser polarization. The laser's influence markedly amplified the electric field around the surface defect, prompting nanoparticles to undergo oxidative growth in all directions due to the near-field effect.

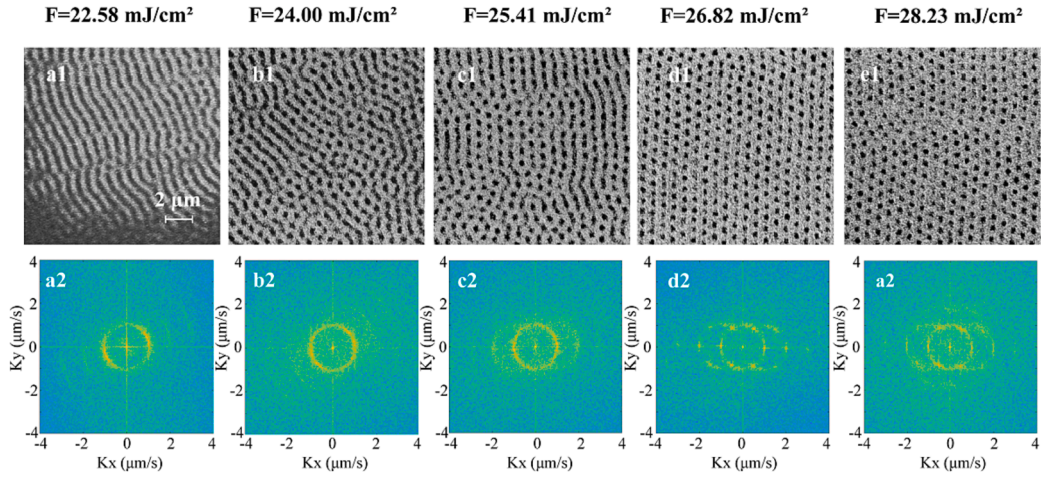

Fig. 2. Evolution of 2D LIPSS on a-Si coated on Al with respect to fluence induced by circularly polarized laser(Up Row). Corresponding fast Fourier transform patterns.

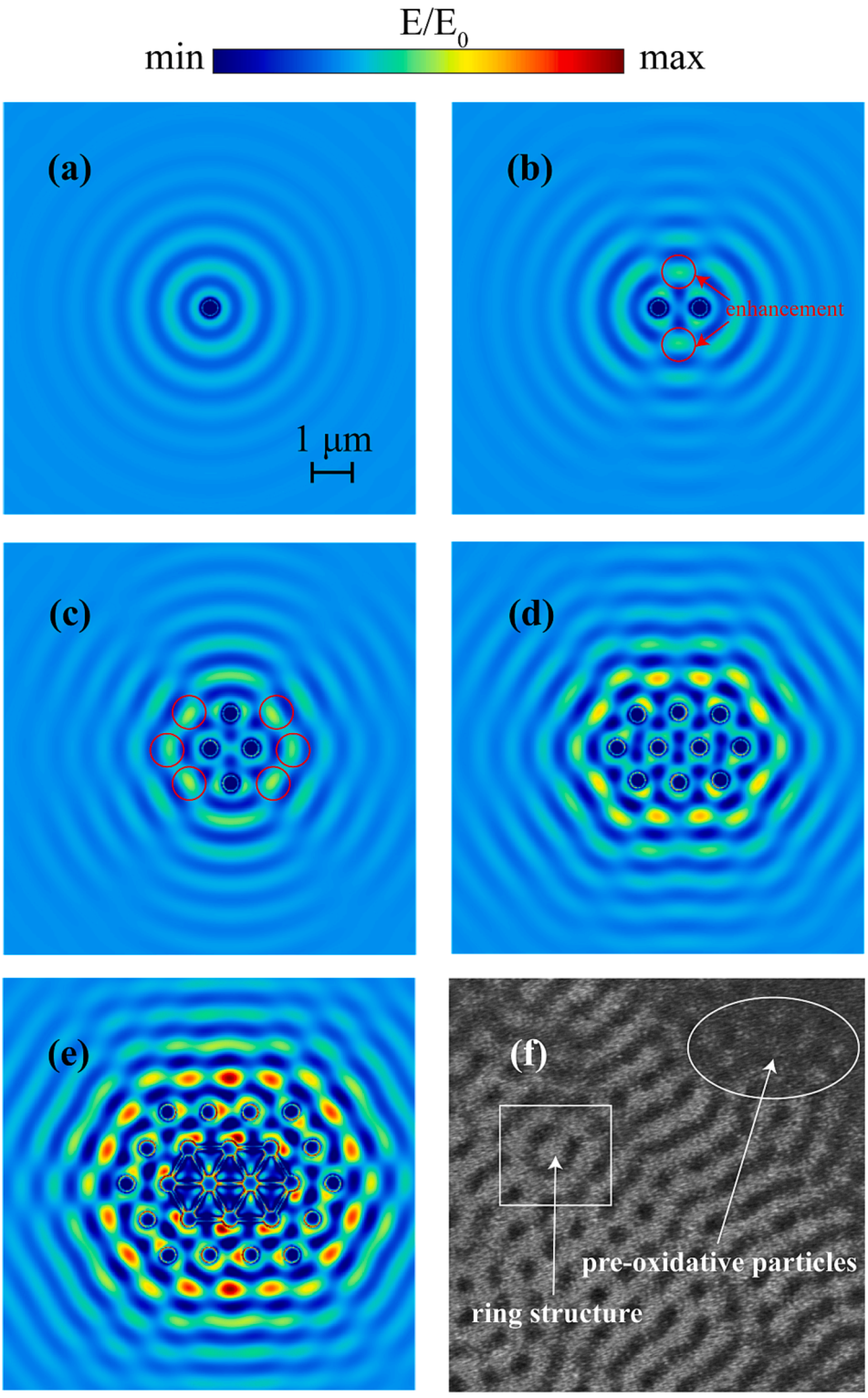

Fig. 3. (a)-(e) Numerical simulations of the growth process of 2D LIPSS on a-Si coated on Al. (f) The ring structure and pre-oxidative particles on a-Si coated on Al when the fluence was 24 mJ/cm$ˆ2$. The scale bar is the same as that of (a).

Concurrently, surface plasmon polaritons (SPPs), excited by surface anomalies, interacted with the laser light on the a-Si surface, crafting a ring-shaped energy intensity distribution. This far-field effect meant a-Si oxidation was most likely at the points of maximum field strength, as seen in the first ring. Yet, practical challenges like surface irregularities and nonlinear competition [37] made the induction of oxidation mode elusive.

The nanoparticles depicted in these simulations represent the natural imperfections and contaminants typically found on film surfaces post-deposition and handling, as confirmed by our AFM characterizations prior to laser treatment (see Figure S 2 in supplementary material). These are not artificially introduced but are inherent to the film deposition process and subsequent handling, playing a pivotal role in the initiation and evolution of LIPSS.

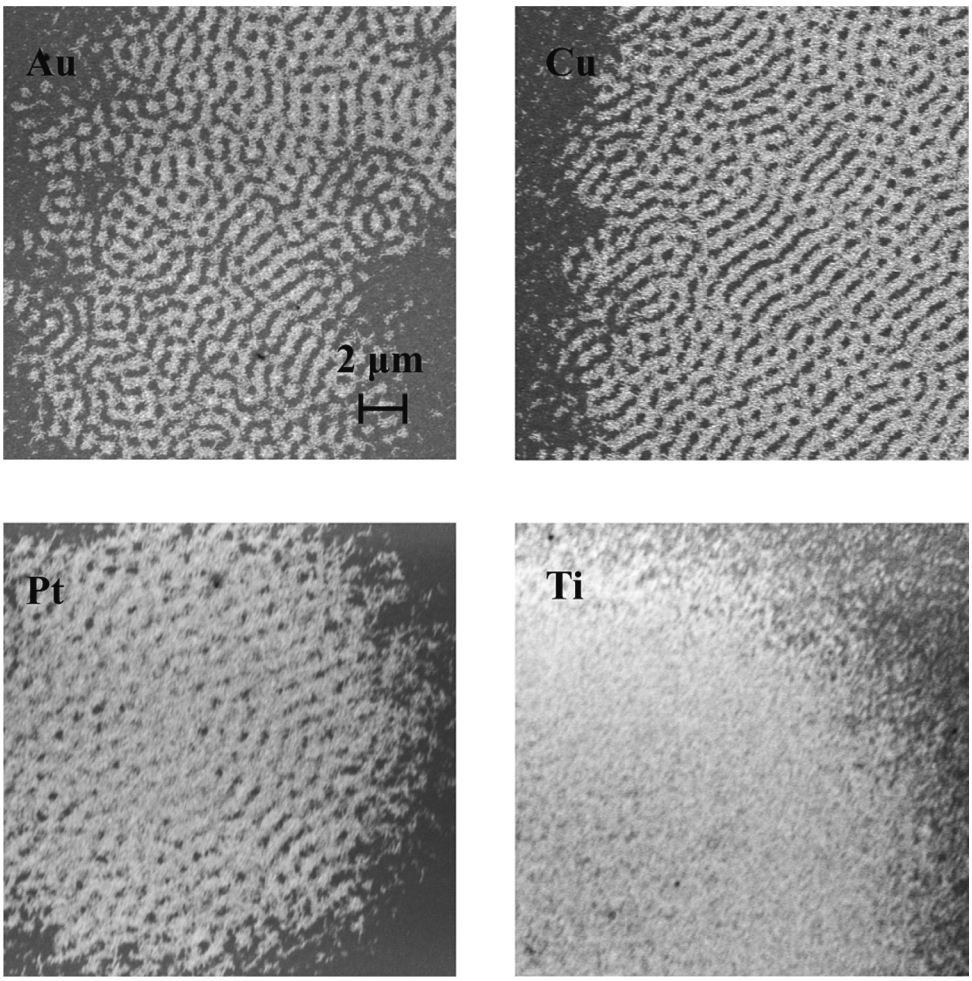

Fig. 4. Optimal Fluence-Induced Patterns on a-Si with Au, Cu, Pt, and Ti Coatings: Characterization Under Circularly Polarized Laser Illumination (Fluences: Au – 23.97 mJ/cm^2, Cu – 25.38 mJ/cm^2, Pt – 36.66 mJ/cm^2, Ti – 56.40 mJ/cm^2).

To elucidate the formation of the hexagonal pattern, we postulate that under appropriate fluence conditions, an oxidative nanoparticle emerges within the confines of the ring, undergoing rapid growth due to the near-field effects. Then, Fig. 3 (b) illustrates how the nanoparticle, in conjunction with the original defect, modifies the field's distribution. Two specific positions, marked by red circles, exhibit increased field strength, becoming primary sites for oxidation. In scenarios with four nanoparticles, as in Fig. 3 (c), oxidation continues to occurs predominantly where the field is strongest. While the far-field effects initiate the oxidative particles, their growth is primarily influenced by the near-field. Fig. 3 (d) highlights the intensified field between adjacent particles, driving them to merge and eventually form ridge structures, as seen in Fig. 3 (e). Areas with field intensity below the oxidation threshold remain unoxidized, leading to hole structures.

The simulations presented in Fig. 3 are not indicative of 'single shot' distributions but rather are intended to model the cumulative effect of multiple laser pulses. The oxidation and pattern formation are progressive, influenced by the continuous application of laser pulses at a high repetition rate (5 kHz), which corresponds to a pulse every 200 microseconds. This rapid succession of pulses collectively contributes to the evolution of the pattern over time.

Laser fluence plays a pivotal role in determining the regularity of LIPSS. While a single nanoparticle induces a symmetric far-field ring pattern, it's the optimal fluence that ensures the evolution to a consistent hexagonal 2D LIPSS. At lower fluences, the oxidation process unfolds gradually and uniformly. This can result in the complete oxidation of the entire far-field peak ring area, as exemplified by the ring structure in Fig. 3 (f). Alternatively, a segment of an arc might undergo uniform oxidation, subsequently altering the distribution of surface electromagnetic waves and culminating in the formation of irregular striped LIPSS. Notably, as shown in Fig. 3 (f), the presence of oxidative particles at the Gaussian beam's periphery underscores that pattern evolution commences from nanoparticles. As fluence escalates, the introduction of multiple, unpredictably induced nanoparticles can further disrupt the pattern's consistency. At a suboptimal fluence of 24 mJ/cm^2, transient features and intermediate states of the pattern formation become observable, providing crucial insights into the underlying mechanisms. Pushing the fluence even higher, as seen at 28.23 mJ/cm^2 in Fig. 2 (e1), leads to the oxidation of the a-Si within the holes. Thus, precise fluence control is crucial for achieving the desired LIPSS regularity.

In the formation of oxidative LIPSS, it's imperative to consider the role of the near-field, a factor that distinguishes it from the formation process of ablative LIPSS. To delve deeper into the interplay between near-field and far-field effects on 2D LIPSS growth on a-Si, we experimented with 50 nm Si films on various 100 nm metals: Au, Cu, Pt, and Ti. Fig. 4 displays the LIPSS patterns induced on a-Si for various metal substrates when using the optimal fluence. For metals with low loss, like Au and Cu, 2D LIPSS formed on a-Si, but the patterns lacked regularity, exhibiting meandering and forked structures. In contrast, with metals exhibiting higher loss, such as Pt, 2D LIPSS were still evident, but with diminished regularity compared to when Al was the substrate. Additionally, the oxidative ridges widened, obscuring the holes. With even higher metal loss, as with Ti, the laser-illuminated area showed no nanostructures but was entirely oxidized.

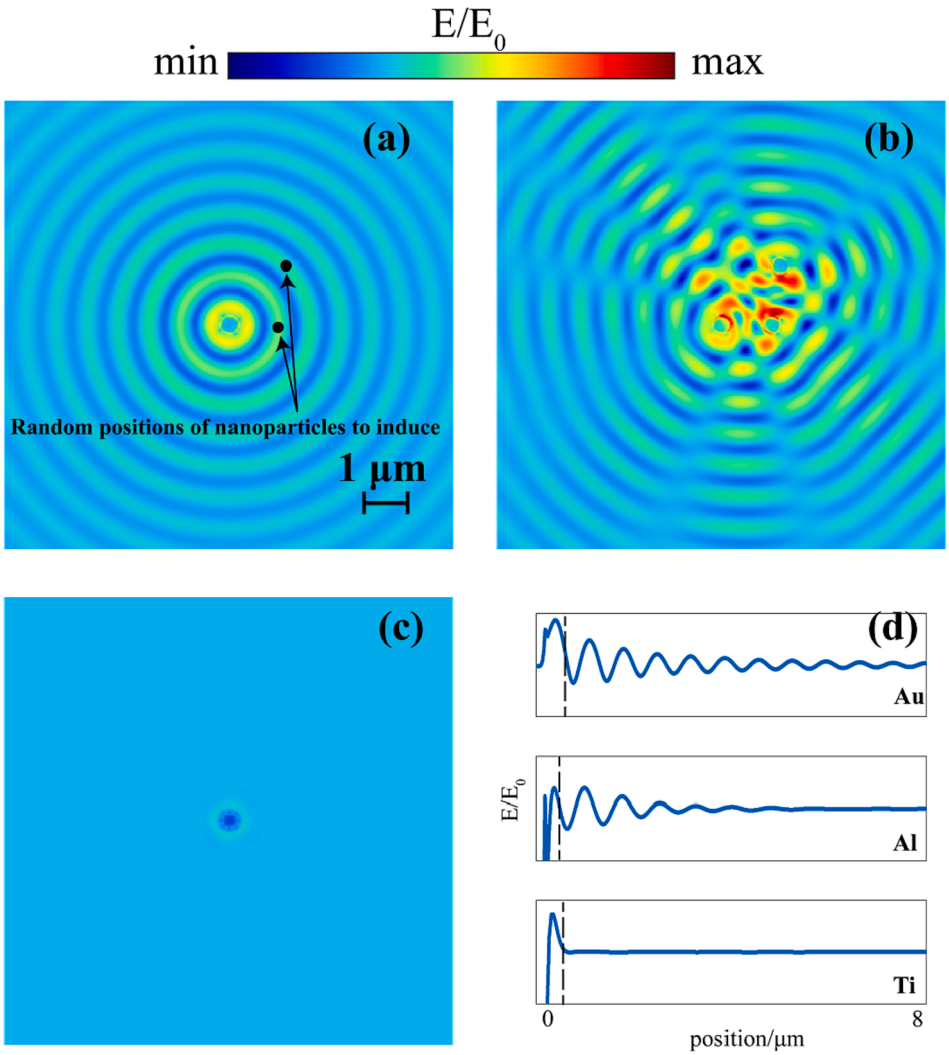

Fig. 5. (a) Simulation of electric field distribution at the Si-air interface caused by a single defect when the underlying metal was Au. (b) Chaotic electric field distribution when nanoparticles were randomly induced on the surface of Si coated on Au. (c) Electric field distribution at the Si-air interface caused by a single defect when the underlying metal was Ti. (d) The relationship of field intensity and distance to the defect when the underlying metal was Au, Al and Ti (single defect case), where the near-field and far-field region were separated by dashed lines.

To further clarify, the terms 'high loss' and 'low loss' used in our study refer to the absorption characteristics of the metal substrates under laser irradiation. 'High loss' metals, such as Ti, exhibit significant absorption of laser energy, leading to enhanced near-field effects and limited propagation of Surface Plasmon Polaritons (SPPs). This results in stronger localized interactions but restricts the reach of the SPPs, influencing the pattern formation. Conversely, 'low loss' metals like Au and Cu, characterized by their lower absorption, allow for extended propagation of SPPs, resulting in different LIPSS characteristics. This distinction is crucial for understanding the varying LIPSS patterns observed on a-Si when coated on different metal substrates.

To understand the impact of different metal losses on 2D LIPSS formation, we turned to numerical simulations. For metals with minimal loss, such as Au, the surface electromagnetic mode pattern was excited by the defect and resembled that of Al, radiating outward in a ring. This pattern for Au is depicted in Fig. 5 (a). Notably, Au's mode exhibited a more extended reach and greater intensity with reduced attenuation, a characteristic evident in Fig. 5 (d). This led to the random induction of oxidative particles at various high-intensity field points. Fig. 5 (b) explores the influence of three nanoparticles on the electromagnetic wave pattern, revealing that the presence of three randomly positioned nanoparticles disrupted the pattern, compromising the large-area 2D LIPSS's long-range regularity. This observation is supported by the numerous oxidized particles seen at the laser spot's edge, as in the Au and Cu cases in Fig. 4.

Conversely, for metals with significant loss, like Ti, the surface electromagnetic wave had a short propagation distance and attenuated swiftly, as shown in Fig. 5 (c). Here, the far-field's contribution paled in comparison to the near-field's. While high-loss metals like Ti enhanced the long-range order in 1D LIPSS induced by linearly polarized lasers [34], they weren't as effective with circularly polarized lasers for 2D LIPSS. The reason lies in the near-field enhancement under circular polarization, which is omnidirectional around the Si-air interface defect, as illustrated in Fig. 5 (c). Although high-loss metals curtailed the far-field's propagation distance and the randomness of oxidative nanoparticle positioning, the overpowering near-field effect caused rapid growth around the defect. Consequently, the entire laser-illuminated area underwent oxidation, bypassing regular LIPSS formation—a finding consistent with our experimental observations with Ti in Fig. 4. Contrasting with the other metals discussed, the Al + Si system uniquely exhibits a harmonious balance between the contributions of both the far-field and near-field. This equilibrium enables the formation of expansive, regular hexagonal LIPSS structures.

In summary, our experiments confirmed the ability to produce a

large-area, regular hexagonal 2D LIPSS on 50 nm a-Si layered over 100 nm Al by meticulously adjusting the circularly polarized laser fluence. We detailed the LIPSS growth mechanism and, through numerical simulations, elucidated the origins of its hexagonal pattern. By juxtaposing experimental and simulated results of LIPSS on a-Si with varying metal substrates, we highlighted the contrasting influences of the near-field and far-field. Specifically, a dominant far-field contribution led to decreased pattern regularity, whereas a pronounced near-field influence resulted in complete oxidation over LIPSS induction. It's evident that achieving long-range ordered LIPSS with a circularly polarized laser, as opposed to a linearly polarized one on a-Si, demands a more precise balance between near-field and far-field intensities.

CRediT authorship contribution statement

Liye Xu: Investigation, Methodology, Validation, Visualization, Writing – original draft, Writing – review & editing. **Jiao Geng:** Methodology, Supervision, Writing – review & editing. **Liping Shi:** Conceptualization, Methodology, Writing – review & editing. **Weicheng Cui:** Writing – review & editing. **Min Qiu:** Supervision, Writing - review & editing.

Declaration of Competing Interest

The authors declare that they have no known competing financial interests or personal relationships that could have appeared to influence the work reported in this paper.

Data availability

No data was used for the research described in the article.

Acknowledgement

This research was funded by the National Key Research and Development Program of China (2022YFC2805200), start-up funding from Westlake University (041030150118), and Scientific Research Funding Project of Westlake University (2021WUFP017).The authors are grateful for the technical support from the Center for Micro/Nano Fabrication and the instrumentation and Service Center at Westlake University. We extend our sincere gratitude to Dr. Zhewei Wang for his invaluable assistance and expertise in the AFM characterization process.

Appendix A. Supplementary material

Supplementary data to this article can be found online at https://doi.org/10.1016/j.apsusc.2023.159100.

References

[1] J. Geng, L. Xu, W. Yan, L. Shi, M. Qiu, High-speed laser writing of structural colors for full-color inkless printing, Nat. Commun. 14 (2023) 565.
[2] R. Zheng, D. Zhao, Y. Lu, S. Wu, G. Yao, D. Liu, M. Qiu, Recording Messages on Nonplanar Objects by Cryogenic Electron-Beam Writing, Adv. Funct. Mater. 32 (2022) 2112894.
[3] J. Geng, L. Shi, J. Ni, Q. Jia, W. Yan, M. Qiu, Wear-resistant surface coloring by ultrathin optical coatings, PhotoniX 3 (2022) 1–11.
[4] V. Zorba, E. Stratakis, M. Barberoglou, E. Spanakis, P. Tzanetakis, S. H. Anastasiadis, C. Fotakis, Biomimetic artificial surfaces quantitatively reproduce the water repellency of a lotus leaf, Adv. Mater. 20 (2008) 4049–4054.
[5] A.-M. Kietziga, M.N. Mirvakilia, S. Kamalb, P. Englezosa, S.G. Hatzikiriakosa, Nanopatterned metallic surfaces: their wettability and impact on ice friction, J. Adhes. Sci. Technol. 25 (2011) 1293–1303.
[6] F.A. Müller, C. Kunz, S. Gräf, Bio-inspired functional surfaces based on laser-induced periodic surface structures, Materials 9 (2016) 476.
[7] X. Jia, T. Jia, N. Peng, D. Feng, S. Zhang, Z. Sun, Dynamics of femtosecond laser-induced periodic surface structures on silicon by high spatial and temporal resolution imaging, J. Appl. Phys. 115 (2014), 143102.
[8] A.I. Kuznetsov, A.B. Evlyukhin, M.R. Gon çalves, C. Reinhardt, A. Koroleva, M. L. Arnedillo, R. Kiyan, O. Marti, B.N. Chichkov, Laser fabrication of large-scale nanoparticle arrays for sensing applications, ACS nano 5 (2011) 4843–4849.
[9] C. Battaglia, J. Escarré, K. Söderström, M. Charriere, M. Despeisse, F.-J. Haug, C. Ballif, Nanomoulding of transparent zinc oxide electrodes for efficient light trapping in solar cells, Nat. Photonics 5 (2011) 535–538.
[10] Y. Lu, A. Lal, High-efficiency ordered silicon nano-conical-frustum array solar cells by self-powered parallel electron lithography, Nano Lett. 10 (2010) 4651–4656.
[11] B.K. Nayak, V.V. Iyengar, M.C. Gupta, Efficient light trapping in silicon solar cells by ultrafast-laser-induced self-assembled micro/nano structures, Progress Photovolt.: Res. Appl. 19 (2011) 631–639.
[12] X. Wang, C.J. Summers, Z.L. Wang, Large-scale hexagonal-patterned growth of aligned ZnO nanorods for nano-optoelectronics and nanosensor arrays, Nano Lett. 4 (2004) 423–426.
[13] W. Wang, M. Ramezani, A.I. V¨akev¨ainen, P. T¨orm¨a, J.G. Rivas, T.W. Odom, The rich photonic world of plasmonic nanoparticle arrays, Mater. Today 21 (2018) 303–314.
[14] X. Zu, B. Chen, N. Tang, E. Wei, J. Wang, M. Qiu, Versatile optical beam routers based on inversely designed supercell metagratings, Photonics and Nanostructures-Fundamentals and Applications 52 (2022), 101075.
[15] A. Ródenas, M. Gu, G. Corrielli, P. Paiè, S. John, A.K. Kar, R. Osellame, Three-dimensional femtosecond laser nanolithography of crystals, Nat. Photonics 13 (2019) 105–109.
[16] Y. Nakata, M. Yoshida, K. Osawa, N. Miyanaga, Fabricating a regular hexagonal lattice structure by interference pattern of six femtosecond laser beams, Appl. Surf. Sci. 417 (2017) 69–72.
[17] B.H. Cumpston, S.P. Ananthavel, S. Barlow, D.L. Dyer, J.E. Ehrlich, L.L. Erskine, A. A. Heikal, S.M. Kuebler, I.-Y.-S. Lee, D. McCord-Maughon, others Two-photon polymerization initiators for three-dimensional optical data storage and microfabrication, Nature 398 (1999) 51–54.
[18] T. Ito, S. Okazaki, Pushing the limits of lithography, Nature 406 (2000) 1027–1031.
[19] Y. Hong, D. Zhao, J. Wang, J. Lu, G. Yao, D. Liu, H. Luo, Q. Li, M. Qiu, Solvent-free nanofabrication based on ice-assisted electron-beam lithography, Nano Lett. 20 (2020) 8841–8846.
[20] P. Li, S. Chen, H. Dai, Z. Yang, Z. Chen, Y. Wang, Y. Chen, W. Peng, W. Shan, H. Duan, Recent advances in focused ion beam nanofabrication for nanostructures and devices: Fundamentals and applications, Nanoscale 13 (2021) 1529–1565.
[21] M. Birnbaum, Semiconductor surface damage produced by ruby lasers, J. Appl. Phys. 36 (1965) 3688–3689.
[22] P. Nürnberger, H. Reinhardt, H. Kim, F. Yang, K. Peppler, J. Janek, N. Hampp, Influence of substrate microcrystallinity on the orientation of laser-induced periodic surface structures, J. Appl. Phys. 118 (2015), 134306.
[23] F. Fraggelakis, G. Mincuzzi, J. Lopez, I. Manek-Hönninger, R. Kling, Controlling 2D laser nano structuring over large area with double femtosecond pulses, Appl. Surf. Sci. 470 (2019) 677–686.
[24] G. Giannuzzi, C. Gaudiuso, R. Di Mundo, L. Mirenghi, F. Fraggelakis, R. Kling, P. M. Lugarà, A. Ancona, Short and long term surface chemistry and wetting behaviour of stainless steel with 1D and 2D periodic structures induced by bursts of femtosecond laser pulses, Appl. Surf. Sci. 494 (2019) 1055–1065.
[25] T.-J.-Y. Derrien, T.E. Itina, R. Torres, T. Sarnet, M. Sentis, Possible surface plasmon polariton excitation under femtosecond laser irradiation of silicon, J. Appl. Phys. 114 (2013), 083104.
[26] E. Rebollar, S. Pérez, J.J. Hernández, I. Martín-Fabiani, D.R. Rueda, T.A. Ezquerra, M. Castillejo, Assessment and formation mechanism of laser-induced periodic surface structures on polymer spin-coated films in real and reciprocal space, Langmuir 27 (2011) 5596–5606.
[27] E. Rebollar, M. Castillejo, T.A. Ezquerra, Laser induced periodic surface structures on polymer films: From fundamentals to applications, Eur. Polym. J. 73 (2015) 162–174.
[28] J. Cui, Rodríguez-Rodríguez,·A., Hernández, M., García-Gutiérrez, M.-C., Nogales, A., Castillejo, M., Mosegui Gonzalez, D., Müller-Buschbaum, P., Ezquerra, T. A., Rebollar, E., Laser-induced periodic surface structures on P3HT and on its photovoltaic blend with PC71BM, ACS Appl. Mater. Interfaces 8 (2016) 31894–31901.
[29] J. Cui, A. Nogales, T.A. Ezquerra, E. Rebollar, Influence of substrate and film thickness on polymer LIPSS formation, Appl. Surf. Sci. 394 (2017) 125–131.
[30] J. Bonse, A. Rosenfeld, J. Krüger, On the role of surface plasmon polaritons in the formation of laser-induced periodic surface structures upon irradiation of silicon by femtosecond-laser pulses, J. Appl. Phys. 106 (2009), 104910.
[31] F. Garrelie, J.-P. Colombier, F. Pigeon, S. Tonchev, N. Faure, M. Bounhalli, S. Reynaud, O. Parriaux, Evidence of surface plasmon resonance in ultrafast laser-induced ripples, Opt. Express 19 (2011) 9035–9043.
[32] I. Gnilitskyi, T.-J.-Y. Derrien, Y. Levy, N.M. Bulgakova, T. Mocek, L. Orazi, High-speed manufacturing of highly regular femtosecond laser-induced periodic surface structures: Physical origin of regularity, Sci. Rep. 7 (2017) 1–11.
[33] P. Nürnberger, H.M. Reinhardt, H.-C. Kim, E. Pfeifer, M. Kroll, S. Müller, F. Yang, N.A. Hampp, Orthogonally superimposed laser-induced periodic surface structures (LIPSS) upon nanosecond laser pulse irradiation of SiO2/Si layered systems, Appl. Surf. Sci. 425 (2017) 682–688.
[34] J. Geng, W. Yan, L. Shi, M. Qiu, Quasicylindrical waves for ordered nanostructuring, Nano Lett. 22 (2022) 9658–9663.
[35] A. Rudenko, C. Mauclair, F. Garrelie, R. Stoian, J.-P. Colombier, Self-organization of surfaces on the nanoscale by topography-mediated selection of quasi-cylindrical and plasmonic waves, Nanophotonics 8 (2019) 459–465.
[36] Y. Fuentes-Edfuf, J.A. Sanchez-Gil, C. Florian, V. Giannini, J. Solis, J. Siegel, Surface plasmon polaritons on rough metal surfaces: Role in the formation of laser-induced periodic surface structures, Acs Omega 4 (2019) 6939–6946.

[37] J. Geng, X. Fang, L. Zhang, G. Yao, L. Xu, F. Liu, W. Tang, L. Shi, M. Qiu, Controllable generation of large-scale highly regular gratings on Si films. Light, Adv. Manuf. 2 (2021) 274–282.
[38] B. Öktem, I. Pavlov, S. Ilday, H. Kalaycıoğlu, A. Rybak, Yava s, S., Erdoğan, M., Ilday, F. O., Nonlinear laser lithography for indefinitely large-area nanostructuring with femtosecond pulses, Nat. Photonics 7 (2013) 897–901.
[39] A. Dostovalov, K. Bronnikov, V. Korolkov, S. Babin, E. Mitsai, A. Mironenko, M. Tutov, D. Zhang, K. Sugioka, J. Maksimovic, others, Hierarchical anti-reflective laser-induced periodic surface structures (LIPSSs) on amorphous Si films for sensing applications, Nanoscale 12 (2020) 13431–13441.
[40] J. Geng, L. Shi, X. Sun, W. Yan, M. Qiu, Artificial Seeds-Regulated Femtosecond Laser Plasmonic Nanopatterning, Laser Photonics Rev. 16 (2022) 2200232.
[41] J. Geng, L. Shi, J. Liu, L. Xu, W. Yan, M. Qiu, Laser-induced deep-subwavelength periodic nanostructures with large-scale uniformity, Appl. Phys. Lett. 122 (2023), 021104.
[42] J. Geng, W. Yan, L. Shi, M. Qiu, Surface plasmons interference nanogratings: wafer-scale laser direct structuring in seconds, Light Sci. Appl. 11 (2022) 189.
[43] Q. Liu, N. Zhang, J. Yang, H. Qiao, C. Guo, Direct fabricating large-area nanotriangle structure arrays on tungsten surface by nonlinear lithography of two femtosecond laser beams, Opt. Express 26 (2018) 11718–11727.
[44] A. Abou Saleh, A. Rudenko, S. Reynaud, F. Pigeon, F. Garrelie, J.-P. Colombier, Sub-100 nm 2D nanopatterning on a large scale by ultrafast laser energy regulation, Nanoscale 12 (2020) 6609–6616.
[45] S. Durbach, N. Hampp, Generation of 2D-arrays of anisotropically shaped nanoparticles by nanosecond laser-induced periodic surface patterning, Appl. Surf. Sci. 556 (2021), 149803.
[46] S. Durbach, H. Kilian, N. Hampp, Laser-driven self-organized evolution of 1D-and 2D-Nanostructures from metal thin-films on silicon: Influence of alloying and oxidation, Appl. Surf. Sci. 622 (2023), 156927.
[47] S. Durbach, F.T. Krauss, M. Hoffmann, V. Lehmann, H. Reinhardt, J. Sundermeyer, N. Hampp, Laser-Driven One-and Two-Dimensional Subwavelength Periodic Patterning of Thin Films Made of a Metal-Organic MoS2 Precursor, ACS nano 16 (2022) 10412–10421.
[48] S.H. van der Poel, M. Mezera, G.-W.-R. Römer, E.G. de Vries, D.T. Matthews, Fabricating laser-induced periodic surface structures on medical grade cobalt–chrome–molybdenum: Tribological, wetting and leaching properties, Lubricants 7 (2019) 70.
[49] J.-M. Romano, A. Garcia-Giron, P. Penchev, S. Dimov, Triangular laser-induced submicron textures for functionalising stainless steel surfaces, Appl. Surf. Sci. 440 (2018) 162–169.
[50] H. Xue, G. Deng, G. Feng, L. Chen, J. Li, C. Yang, S. Zhou, Role of nanoparticles generation in the formation of femtosecond laser-induced periodic surface structures on silicon, Opt. Lett. 42 (2017) 3315–3318.
[51] H. Van Driel, J. Sipe, J.F. Young, Laser-induced periodic surface structure on solids: A universal phenomenon, Phys. Rev. Lett. 1982 (1955) 49.
[52] J. Sipe, J.F. Young, J. Preston, H. Van Driel, Laser-induced periodic surface structure. I. Theory, Phys. Rev, B 27 (1983) 1141.